IOP Publishing | International Atomic Energy Agency Nuclear Fusion

Nucl. Fusion **57** (2017) 016038 (12pp) doi:10.1088/1741-4326/57/1/016038

# Ion radiation albedo effect: influence of surface roughness on ion implantation and sputtering of materials

**Yonggang Li**[1,2,4], **Yang Yang**[2], **Michael P. Short**[2], **Zejun Ding**[3], **Zhi Zeng**[1,4] **and Ju Li**[2,5]

[1] Key Laboratory for Materials Physics, Institute of Solid State Physics, Chinese Academy of Sciences, Hefei 230031, People's Republic of China
[2] Department of Nuclear Science and Engineering, Massachusetts Institute of Technology, Cambridge, MA 02139, USA
[3] Hefei National Laboratory for Physical Sciences at Microscale and Department of Physics, University of Science and Technology of China, Hefei 230026, People's Republic of China
[4] University of Science and Technology of China, Hefei 230026, People's Republic of China
[5] Department of Materials Science and Engineering, Massachusetts Institute of Technology, Cambridge, MA 02139, USA

E-mail: zzeng@theory.issp.ac.cn, hereiam@mit.edu and liju@mit.edu

Received 30 June 2016, revised 7 October 2016
Accepted for publication 17 October 2016
Published 8 December 2016

**Abstract**

In fusion devices, ion retention and sputtering of materials are major concerns in the selection of compatible plasma-facing materials (PFMs), especially in the context of their microstructural conditions and surface morphologies. We demonstrate how surface roughness changes ion implantation and sputtering of materials under energetic ion irradiation. Using a new, sophisticated 3D Monte Carlo (MC) code, IM3D, and a random rough surface model, ion implantation and the sputtering yields of tungsten (W) with a surface roughness varying between 0–2 $\mu$m have been studied for irradiation by 0.1–1 keV $D^+$, $He^+$ and $Ar^+$ ions. It is found that both ion backscattering and sputtering yields decrease with increasing roughness; this is hereafter called the ion radiation albedo effect. This effect is mainly dominated by the direct, line-of-sight deposition of a fraction of emitted atoms onto neighboring asperities. Backscattering and sputtering increase with more oblique irradiation angles. We propose a simple analytical formula to relate rough-surface and smooth-surface results.

Keywords: ion radiation albedo effect, surface roughness, ion implantation and sputtering, plasma-facing materials, Monte Carlo

S Online supplementary data available from stacks.iop.org/NF/57/016038/mmedia

(Some figures may appear in colour only in the online journal)

## 1. Introduction

Ion beam and plasma processing are widely used to tailor the geometric, mechanical, electronic, magnetic, and optical properties of materials [1, 2]. Ion irradiation induces serious radiation damage [3, 4], while plasma-surface interactions affect the lifetime of the plasma-facing materials (PFMs) in fusion reactors by inducing changes in surface roughness and thermal transport; this potentially evaporates the PFMs and causes them to degrade or quench the core plasma. Ion (D/T/He) retention and sputtering of PFMs are therefore major concerns in the selection of compatible PFMs in fusion reactors [5–8]. PFMs in proposed fusion reactors must withstand low-energy (10–1000 eV), high-flux (up to $10^{24}$ $m^{-2}$ $s^{-1}$) D/T/He ions, high-energy neutrons (14.1 MeV) as well as high heat fluxes up to 20 MW $m^{-2}$ [7]. The surface morphology of

PFMs is dramatically modified, forming features like mounds, fuzz, bubbles, pores, and blisters [8]. These surface features, with a characteristic length scale $L_R$ comparable to the ion penetration depth $L_I$, can significantly affect the ion retention and sputtering of PFMs. This in turn affects the further evolution of PFM surfaces, creating a complex, positive-feedback evolution of PFM surface roughness.

In general, tungsten (W) surface features under high fluxes of low-energy He-ion irradiation are attributed to bubble bursting and/or loop punching caused by He-induced void growth and physical sputtering [9, 10]. High implantation of He atoms is also one of the key factors that generate bubble growth, as inert gases stabilize radiation void nuclei, and the subsequent formation of 'tungsten fuzz' [11]. He-induced W surface nanostructures have thus been recognized as a potential drawback for W as a PFM, due to their inducing fragility, degrading thermal transport, and the potential enhancement of ion/fuel retention [12]. In a different context, techniques which employ surface structuring by energetic ion bombardment, including ion beam sputtering [13] and low-energy He-ion irradiation [2], are established surface processing techniques. For example, due to their high porosity (up to 90%), surface fuzzy structures manifest their potential in various applications requiring high surface area and light absorption [2, 14]. However, the resulting complex surface morphology and its effects on surface sputtering and erosion, H-isotope trapping and release, have not been fully addressed [15]. Experimental studies show that it is rather difficult to rely on a single quantity to predict the behavior of materials after ion/plasma exposure [2]. It is therefore essential to understand the fundamental and practical aspects of irradiated materials in the context of their microstructural conditions and surface morphologies [15].

Recent studies have found that ion retention [16] and physical sputtering [2, 12, 17–21] respectively increase and decrease due to surface roughening, causing the material to behave more like a "sponge" or "dark body". While the behaviors of ion retention and sputtering of smooth materials under different conditions have been well studied, including ion energy [6], flux [22], fluence [22, 23], incident angle [24], sample temperature [22–24] and existing defects [24], much less is known regarding the effects of surface roughness and porosity on ion retention/implantation and sputtering of materials [16, 25]. Because $L_I$ is typically 1–10 nm, surface nanoporosity or nanofeatures should change a surface's ion 'albedo' or 'darkness', and also its ion 'matte' or 'gloss'.

Recently, the enhancement of ion retention by surface roughness has been indicated by deuterium (D) retention experiments in pre-damaged W [16]. Trapping of significant amounts of D should take place in or close to the blister/protrusion in W pre-damaged by implantation with MeV ions, and give rise to an additional peak in the thermal desorption spectrum at 700 K [16]. This increased D retention is mainly caused by the creation of defect sites/sinks like dislocations around the blister cavities. In general rough surface features reduce D retention due to shorter diffusion pathways to the surface and thus higher D effusion from these surfaces. The influence of roughness on out-diffusion is larger than that on implantation. But if the contribution of D diffusion and trapping to desorption is fixed, the ion implantation increase would be the only key factor left to affect D retention. Reduced sputtering from rough/fuzzy surfaces has also been recently reported. Based on mass loss measurements, Nishijima *et al* have shown that the sputtering yield of fuzzy W surfaces under 110 eV Ar-ion sputtering decreases with increasing fuzz thickness and saturates at about 10% of that of a smooth surface [12]. They attributed the reduction in sputtering yield to the direct line-of-sight deposition of sputtered W atoms onto neighboring fuzz before ejection into the plasma. Tanyeli *et al* also showed that their measured values of the sputtering yield of metals with He-induced surface modifications are around one order of magnitude below the expected one, due to the effect of surface morphology [2]. Doerner *et al* [18–21] have systematically investigated the influence of surface morphology on the sputtering of beryllium (Be), for pure Be exposed to high-flux [18] and high-fluence [19] un-seeded [19] or Be-impurity-seeded D plasma [18, 20, 21] at room or elevated temperatures [21]. They also found that Be erosion by D plasma results in the development of a cone/grass-like surface morphology. The resultant measured erosion rate is almost an order of magnitude less than expected from simple sputtering calculations, mainly due to the deposition of some sputtered atoms on adjacent cones.

In fact, at energies sufficiently above the sputtering threshold energy, Sigmund's theory already proposes curvature-dependent sputtering [26]. Based on Sigmund's theory, and assuming symmetric surface structures, an analytical formula for a morphology-dependent sputtering yield predicts a decrease in the sputtering yield with curvature [17]. However, real morphological changes are more complex than a symmetrical structure defined by a finite number of parameters, thus a larger deviation between calculated and experimental data is expected [2].

Therefore, modeling the relations between ion-implantation increase/sputtering decrease and surface-roughness evolution is necessary, though computationally challenging. Monte Carlo (MC) simulations can predict some ion implantation and sputtering behavior, showing the effects of roughness on the sputtering yield [27–31]. In particular, fractal rough surface models have been introduced into MC simulations [29–31] to capture more features of rough surfaces. Ruzic added fractal geometry composed of an exact self-similar fractal into the VF-TRIM code [29]. Kenmotsu *et al* also incorporated a 2D fractal surface model into their ACAT code [30], and set the fractal dimension to 2.1 to fit the experimental data. Recently, Hu and Hassanein developed a new fractal version of ITMC-F to study the impact of the surface roughness on the angular dependence of sputtering yields; this was based on random fractal surfaces generated by a midpoint displacement algorithm in computer graphics and a support vector machine algorithm in pattern recognition [31]. However, these fractal rough-surface models are either quite simplified with the overall effect being other than the local effect of fractal rough surfaces [29], or are relatively more complicated, with several adjustable fitting parameters [30, 31]. Established common codes like SRIM [32] still cannot treat heterogeneities structures, such as nanostructures and roughness. In addition, nearly all of these models emphasize the influence of the incident angles on sputtering. Thus, the dependence of ion implantation and sputtering yields on the surface roughness should be studied more realistically and systematically.

By using the new IM3D code [33], a general and robust approach has been developed to analyze ion-radiation damage and the corresponding 3D spatial distributions of primary defects in nanostructured materials under ion-beam irradiation. In this work, we propose a general rough-surface geometry model based on the finite element triangular mesh (FETM) algorithm [34] and successfully couple it into IM3D, creating a way to reveal the effects of surface roughness on ion implantation and sputtering in detail. Note that IM3D can track processes (like ion implantation and sputtering) at timescales of less than about 10 ps in general. Other key processes at longer timescales, namely the formation of surface roughness in conjunction with the erosion and deposition by the incident beam, are beyond the scope of this paper and are not investigated.

## 2. Methods

All simulations are performed with IM3D [33] using the 'full cascades (FC)' option, as shown below. This is always adopted to follow the tracks of all ions and subsequent cascades using binary collision approximation, since the 'quick Kinchin–Pease (QKP)' [35, 36] option does not produce information regarding the angular distribution of sputtered atoms. In addition, when the material feature size scale becomes nano-scale, the nano-energetic and nano-geometric effects can take place in collision cascades, as discussed in the supplementary online material (SOM 1) (stacks.iop.org/NF/57/016038/mmedia). For objects smaller than 20 nm, both of these two effects must be taken into account, while for objects >20 nm, the nano-energetic effect is less important. Since in most cases the feature size of the roughness/fuzz induced by irradiation is larger than 20 nm [37], the nano-energetic effect may be neglected.

### 2.1. IM3D code

An open-source, parallel, 3D MC code, IM3D, is developed for simulating the transport of ions through and the production of defects within nanostructured materials with excellent parallel scaling performance [33]. IM3D is based on fast indexing of scattering integrals and the SRIM stopping power database, and allows the user a choice of constructive solid geometry (CSG) [38, 39] or the FETM [34, 40] method for constructing 3D shapes and microstructures. It can thus model arbitrarily complex 3D targets made of different geometric elements, each composed of different materials. In addition, the generation of point defects (i.e. interstitials and vacancies) can be modeled alternatively by the 'QKP' [35, 36] and 'FC' options. Both the 3D spatial distribution of ions and also the kinetic phenomena associated with the ions' energy loss, such as amorphization, damage, sputtering, ionization, and phonon production, can be calculated rapidly by IM3D while following all target atom cascades in detail. Different output parameters can thus be given, including electronic and nuclear energy deposition, back-scattering/implanted ions, radiation dose in DPA (displacements per atom), point defect concentrations, and sputtered atoms, etc. For 2D films and multilayers, IM3D perfectly reproduces SRIM calculation results, and can be ~$10^2$ times faster in serial execution and $>10^4$ times faster using a Beowulf parallel computer. For 3D problems, it provides a fast approach for analyzing the spatial distributions of primary displacements and defect generation under ion irradiation. In general, a typical simulation of $10^5$ ions in total with energies of keV to MeV consumes only seconds to minutes on a Beowulf cluster, even for complex 3D geometry.

### 2.2. Rough-surface generation

A simple rough-surface geometry model based on the FETM approach is chosen here, reproducing the typical features of a rough surface, as shown in SOM 2. Specifically, the height of each mesh point, $Z$, on a square mesh with lattice constant $a$ (figure 1(*a*)), is sampled following the truncated Gaussian distribution:

$$f(Z) \propto \exp(-Z^2/2\sigma^2),\ Z \in [-3\sigma, 3\sigma]\,. \tag{1}$$

Each square is then divided into two triangular elements by randomly selecting diagonal directions to generate a triangular mesh, as shown in figure 1(*a*). Each peak/valley in a complex polyhedron form is built according to the random height of each mesh point (figure 1(*b*)), and an isotropic rough-surface mesh is thus constructed, as shown in figure 1(*c*). An ensemble of rough surfaces can be constructed by adjusting $3\sigma$ and $a$. When $3\sigma = 0$ nm, the limiting case of a smooth surface is generated.

Compared to the fractal rough surface model [29–31], this FETM-based geometry model [34] is simpler and more intuitive, and can even reproduce realistic rough surfaces according to the experimental AFM images with only two adjustable parameters ($3\sigma$ and $a$) [41]. Furthermore, it is also a feasible and efficient framework for performing IM3D simulations, which can represent real scattering trajectories near rough surfaces and simultaneously take into account of the refraction effect of ongoing particles with respect to the local surface normal [33, 34].

## 3. Results

### 3.1. Trajectories of ions, recoils and sputtered atoms

The effects of factors like roughness ($\sigma$) and angle of incidence ($\theta$) on the primary ion backscattering coefficient ($\eta_0$) and sputtering yield ($Y$) can therefore be quantitatively simulated. During irradiation, some of the incident ions enter and remain in the matrix, while a fraction $\eta_0$ are backscattered from the surface, as shown in figure 2(*a*). In addition, cascade damage in the matrix and sputtering near the surface occur when the incoming ion energy is high enough. These physical processes are shown in figures 2(*b*) and (*c*) by tracking the trajectories of ions as well as recoil and sputtering atoms for

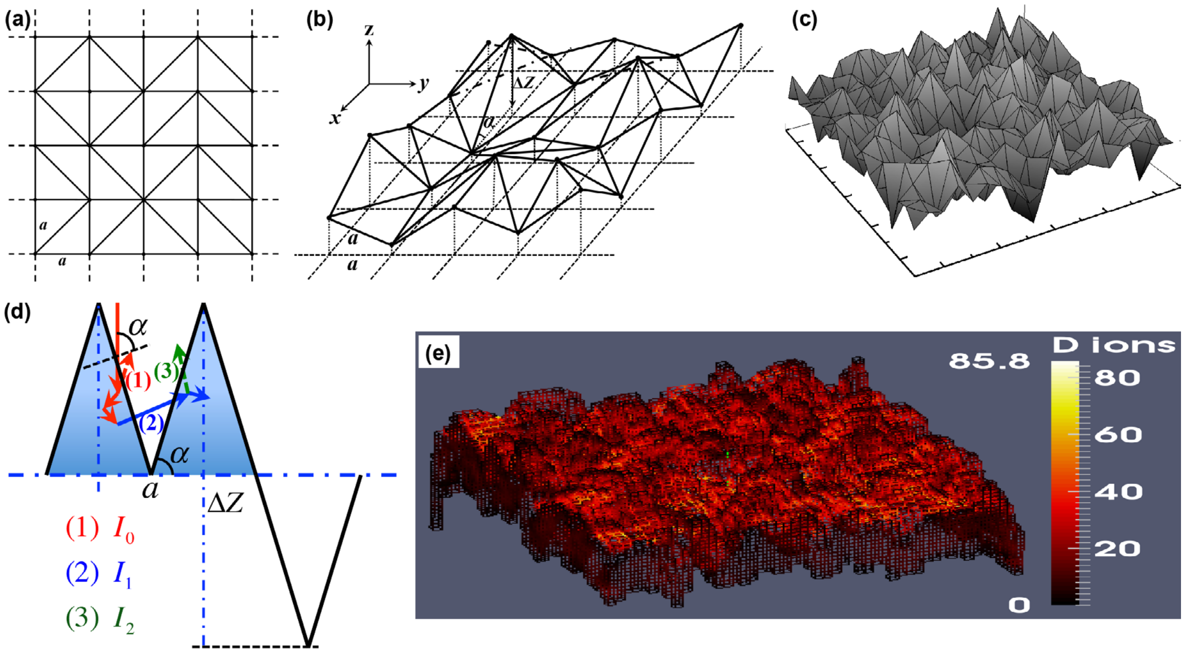

**Figure 1.** (*a*) Schematic of the triangular mesh and (*b*) the polyhedra forming rough peaks. (*c*) A rough surface constructed by the FETM method, and (*d*) a typical cross section of the asperities. (1) $I_0$, (2) $I_1$, and (3) $I_2$ indicate the first backscatters of incident ions from a rough peak, the shading of backscattered ions by an adjacent rough peak, and the secondary backscattering of shaded ions from the adjacent rough peak, respectively. (*e*) The spatial distribution of D-ion implantation in W rough surface with $3\sigma = 60\,\text{nm}$ and $a = 50\,\text{nm}$.

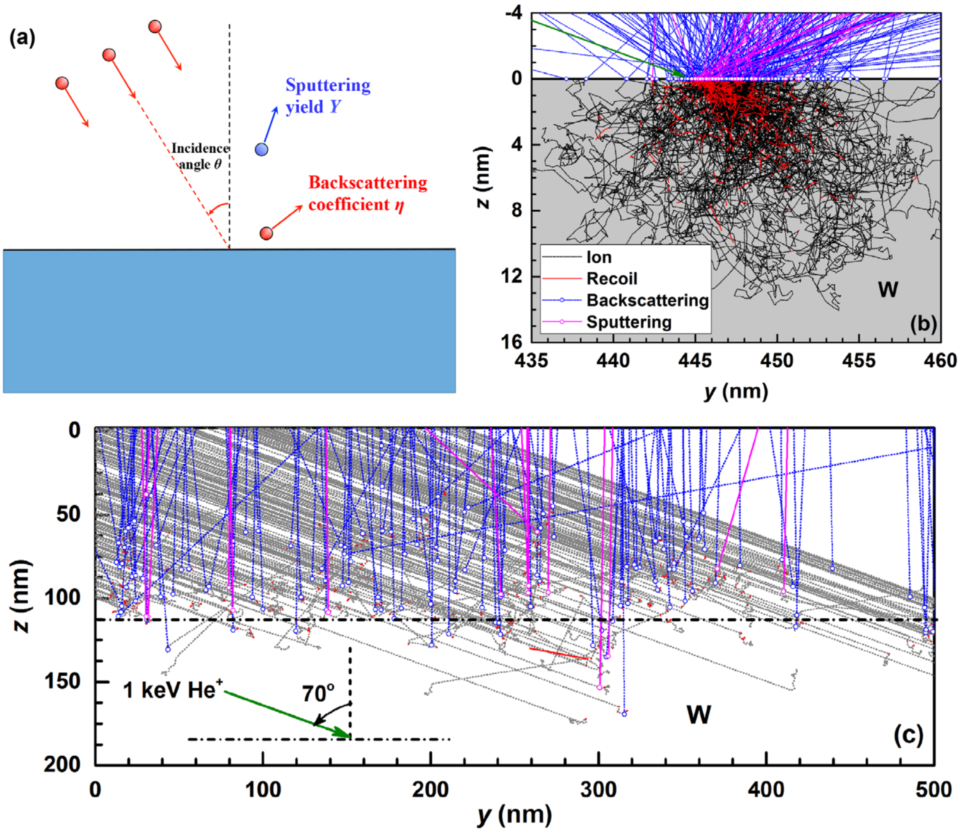

**Figure 2.** (*a*) Schematic of ion incidence, backscattering and sputtering processes. The trajectories of ions, recoils, and sputtered atoms for both (*b*) smooth ($3\sigma = 0$ nm) and (*c*) rough ($a = 50\,\text{nm}$, $3\sigma = 100\,\text{nm}$) W surfaces for 300 1 keV He ions at an incident angle of 70° are shown. Single point and random square ion beams are used for the smooth and rough surfaces, respectively. All trajectories are projected onto the $y$–$z$ plane. The scale difference between (*b*) and (*c*) is due to the large mismatch between the ion penetration depth $L_I$ (about 12 nm) and the spread characteristic length scale $L_R$ (about 200 nm) of the rough surface.

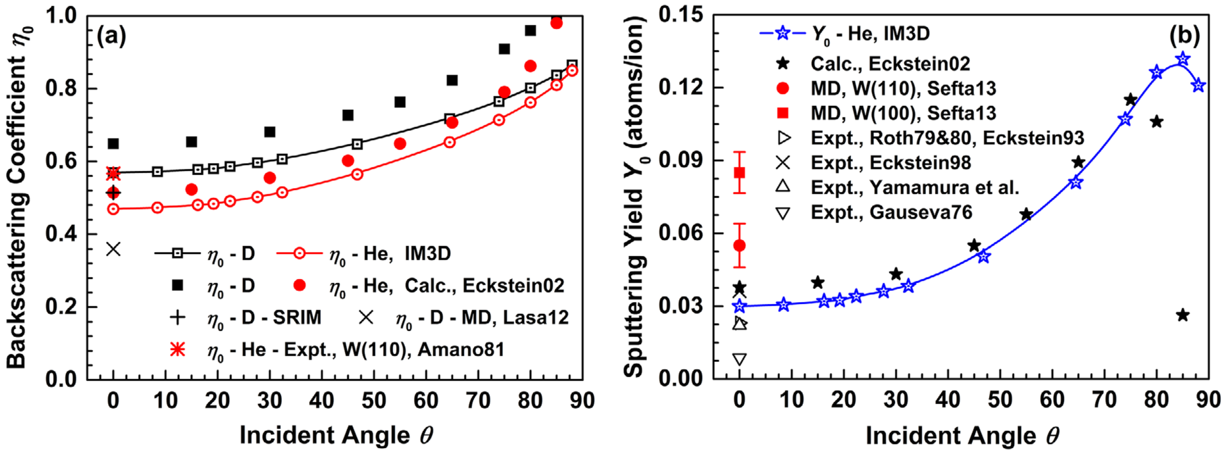

**Figure 3.** Incident polar angle ($\theta$) dependent (*a*) backscattering coefficient ($\eta_0$) and (*b*) sputtering yield ($Y_0$) of 100 eV D/1 keV He-ion bombardment of smooth W surface ($3\sigma = 0$ nm). The SRIM (calculated by SRIM-2013 [32] with default settings), TRIM.SP [42, 43] and MD [48] values of the D backscattering coefficient, the TRIM.SP [42, 43] and experimental values [49] of the He backscattering coefficient as well as the TRIM.SP [42], MD [46, 50] and experimental values [51–58] of the He sputtering yields for a smooth surface are also given for comparison. Spline fitting lines are also drawn to guide the reader's eye.

W bulk with both smooth ($3\sigma = 0$ nm) and rough ($a = 50$ nm, $3\sigma = 100$ nm) surfaces. At glancing incidence ($\theta = 70°$), most of the backscattered ions and sputtered atoms can escape from the smooth surface, while for the rough surface they are re-intercepted by the rough peaks ('shading effect'). Only a small fraction of them may escape, nearly vertically from the rough surface. Thus, the roughness $\sigma$ and incident angle $\theta$ are two key factors, as discussed in detail below. Also, the angular distributions of backscattered ions and sputtered atoms also depend on the roughness, giving the 'albedo' and 'matte' properties, as in optics.

### 3.2. Smooth W surface

The smooth W surface ($3\sigma = 0$ nm) is examined first as a reference. The $\theta$-dependent backscattering coefficient ($\eta_0$) and sputtering yield ($Y_0$) under 100 eV D- or 1 keV He-ion bombardment are calculated by IM3D, as shown in figure 3. Both $\eta_0$ and $Y_0$ increase with increasing $\theta$, except for a small decrease in $Y_0$ for $\theta > 85°$. The trend is consistent with previous analytical [17], simulation [42–46] and experimental results [45, 47], but with the absolute values a little lower than that of Eckstein, except for $Y_0$ at glancing incidence. Note that we have taken into account the refraction effect at surfaces/interfaces in IM3D, which should decrease the probability of ion outgoing from surface especially at glancing incidence. Low-ion backscattering further causes the increases of sputtering yields, thus resulting in a higher value of $Y_0$ at glancing incidence by IM3D compared to that of Eckstein. The absolute value of $\eta_0 = 0.57$ for 100 eV D ions at normal incidence ($\theta = 0$) is a little higher than that of MD [48] due to the exclusion of the channeling effect, and is reasonably located between values obtained by SRIM-2013 [32] and TRIM.SP [42, 43] due to the differences in the detailed treatment of ion scattering and geometry framework in IM3D. The absolute value of $\eta_0 = 0.47$ atoms/ion for 1 keV He ions at $\theta = 0$ is in a reasonable range when compared with TRIM.SP [42, 43] and experiment [49]. The absolute value of $Y_0 = 0.03$ atoms/ion for 1 keV He ions at $\theta = 0$ is reasonably located between the values obtained by TRIM.SP [42], MD [46, 50] and experiments [51–58]. Here, default settings are used for simulating 100 eV D-ion bombardment of W by SRIM-2013 [32]. Note that Eckstein's data compilation [42, 43, 53, 59] is usually considered the gold standard for ion reflection and sputtering. SRIM calculations [32] have some issues like the misestimate of displacement damage [33, 60], the wrong angular distribution of sputtered atoms for targets containing low $Z$ elements [45] and limitations in simulating sputtering yield close to the threshold energy [61]. In any case, the absolute values of $\eta_0$ and $Y_0$ will not affect the strength of the nano-geometric effect, as shown below.

The angular distributions of outgoing ions/atoms' polar ($\theta'$) and azimuthal ($\phi'$) angles for both backscattered and sputtered W atoms are shown in figure 4. The polar angle distribution of outgoing ions/atoms for $\theta = 0$ (red line in figures 4(*a*) and (*e*)) shows a characteristic sine relationship, $A\sin(2\theta')$, as indicated in previous studies [44, 62]. In addition, the most probable $\theta'$ increases with $\theta$, which is also consistent with MD simulations [44]. The $\phi'$ distribution of backscattered ions is uniform for $\theta = 0$ [44], but it becomes more and more anisotropic with increasing $\theta$. Compared to D ions, the peaks in the $\theta'$, $\phi'$ distributions of backscattered He ions are a little sharper. The $\theta'$ and $\phi'$ distributions of sputtered W atoms under 1 keV He-ion irradiation also follow similar trends except for three minor differences: (a) the most probable outgoing $\theta'$ is 55° at $\theta > 70°$, (b) a broader peak of $\phi'$ is near the value of $\theta$, and (c) a small decrease appears at glancing incident angles, as shown in figure 3(*b*). The sputtering yields, which first increase and then decrease with increasing $\theta$, as well as the anisotropic distribution of sputtering atoms at glancing incidence, are consistent with other predictions [42–45, 53, 59].

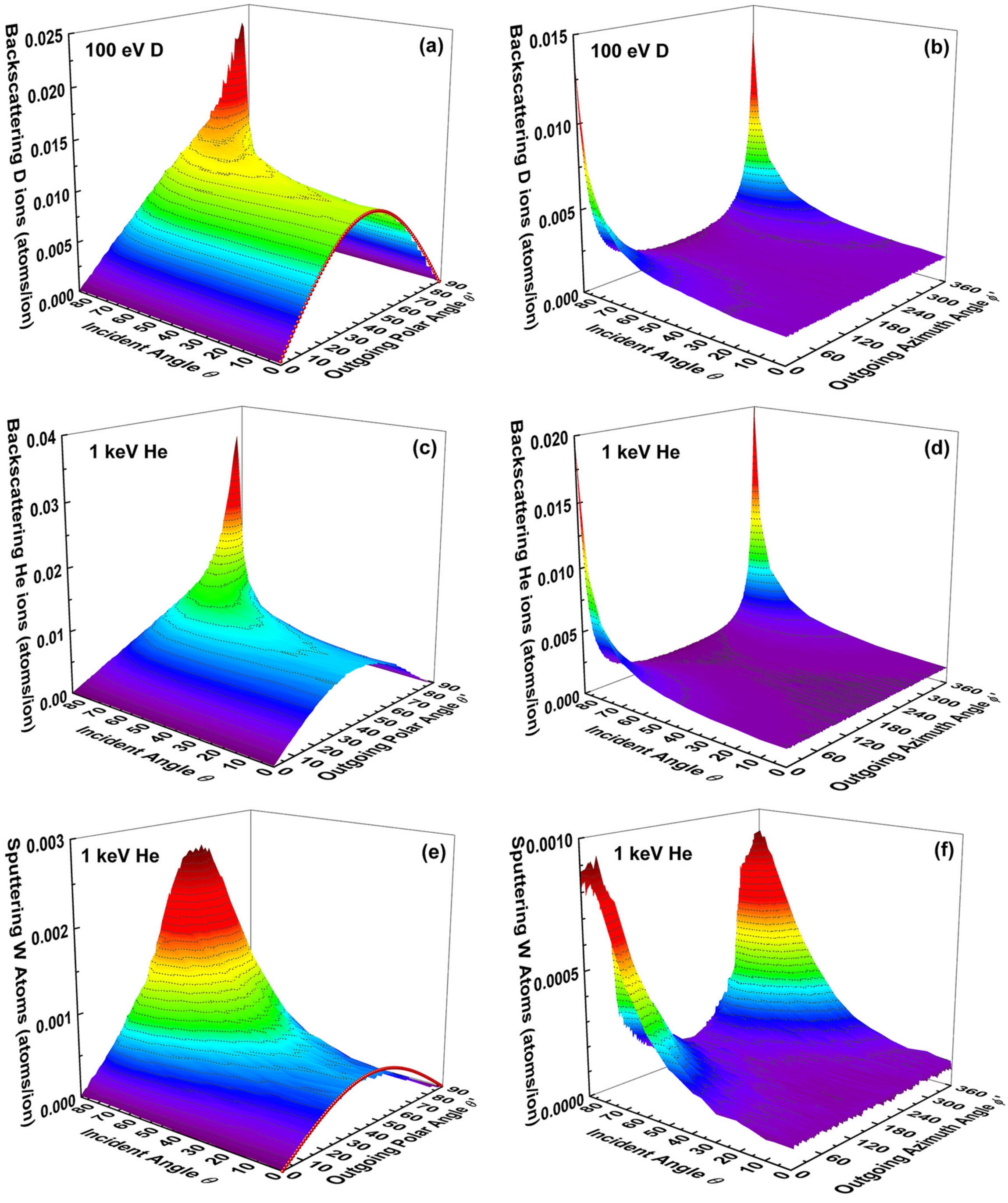

**Figure 4.** (*a*) Polar ($\theta'$) and (*b*) azimuthal ($\phi'$) angle distributions of backscattered D ions from smooth W surface under 100 eV D-ion irradiation with different incident angles ($\theta$). (*c*) $\theta'$ and (*d*) $\phi'$ distributions of backscattered He ions, and (*e*) $\theta'$ and (*f*) $\phi'$ distributions of sputtered W atoms from smooth W surface under 1 keV He-ion irradiation with different $\theta$. The red lines in (*a*) and (*e*) show a sine fit to $\theta'$ at normal incidence ($\theta = 0$).

### *3.3. Rough W surface*

First, 100 eV D-ion irradiation with finite surface roughness ($3\sigma = 0$–$1000$ nm, $a = 50$ nm) is simulated. The 3D spatial distribution of D-ion implantation I=$1-\eta$ (i.e. the fraction of D-ion deposition in W to total D fluence) in the W surface is shown in figure 1(*e*). D ions are mainly distributed in the near-surface region, several nm deep, and fluctuate along with the rough peaks and valleys. The depth distribution of D in rough W at normal incidence and the relation of $I$ to $3\sigma$ and $\theta$ are shown in figures 5(*a*) and (*b*), respectively. The D ion depth distribution follows a Gaussian function, whose full width at half maximum (FWHM) increases with increasing $3\sigma$ and also nearly equals the FWHM of the surface roughness. This illustrates that the nano-geometric effect mainly influences ion implantation, and the ion penetration depth is just another small contribution. As shown in figure 5(*b*), $I$ increases with increasing $3\sigma$ and decreases with increasing $\theta$. It is dominated by the interplay of backscattering enhancement with

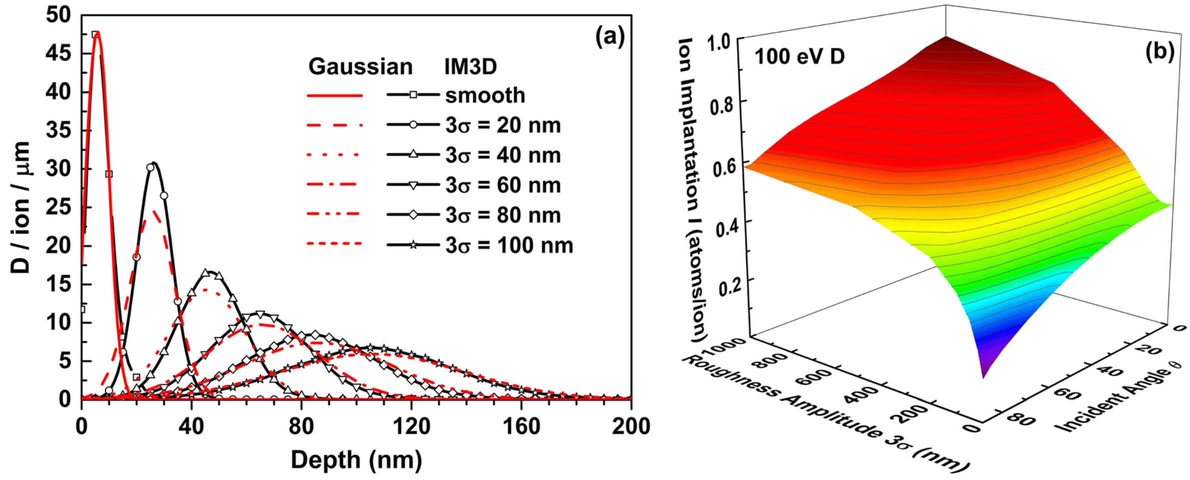

**Figure 5.** (*a*) D-ion depth distributions (black lines) for W rough surface with $3\sigma$ varying from 0–100 nm and $a = 50$ nm, under 100 eV random D-ion irradiation at normal incidence ($\theta = 0$). The depth distribution of D is obtained by integrating D spatial distribution along the two orthogonal directions parallel to the surface. The red lines show the convolution of the Gaussian function with $\sigma$ and D-ion depth distribution for a smooth W surface. Here '0' depth is defined as $Z$ equal to -$3\sigma$, referring to the mean height of surface roughness. (b) D-ion implantation $I$ for W rough surface with $3\sigma$ varying from 0–1000 nm and $a = 50$ nm, under the irradiation of a 100 eV random D-ion beam with different incident polar angles ($\theta$).

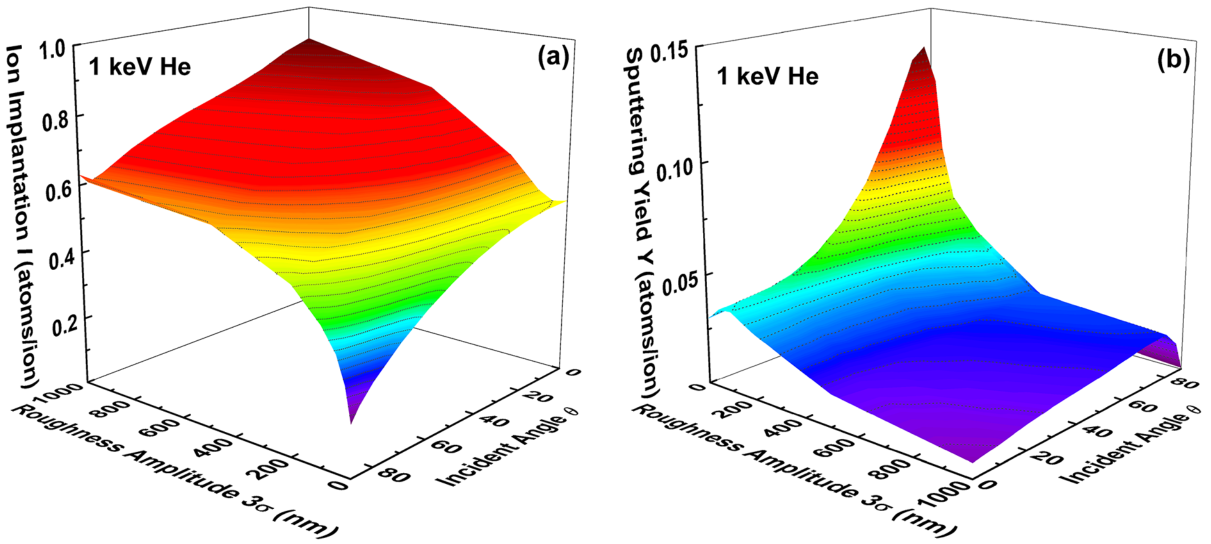

**Figure 6.** (*a*) He-ion implantation $I$ and (*b*) sputtering yields $Y$ for a W rough surface with $3\sigma$ varying from 0–1000 nm and $a = 50$ nm, under irradiation by 1 keV randomly-oriented He ions with different incident polar angles ($\theta$).

the effective incident angles $\alpha$ (related to $3\sigma$ and $\theta$) and the shading effect by rough peaks for different roughness, as mentioned in the next section.

Next, 1 keV He-ion sputtering of W is simulated using the same geometry, with the results given in figure 6. The same trend of increasing He-ion implantation with roughness and incident polar angles is shown in figure 6(*a*). Surface sputtering would occur when the energy of He ions used is high enough (>107 eV). Accordingly, the variation of $Y$ with $3\sigma$ and $\theta$ is shown in figure 6(*b*). The opposite trend is found compared to the relationship between $I$ and $3\sigma$ and $\theta$. $Y$ for He ions decreases with increasing $\sigma$, which is consistent with recent experiments (as shown in figure 7) [2, 12] except for a minor increase for $3\sigma < 50$ nm at small $\theta$. The minor increase of $Y$ for $3\sigma < 50$ nm at small $\theta$ is mainly due to the domination of sputtering enhancement compared to the shading suppression. The reduction of $Y$ with increasing $\sigma$ comes mainly from the direct line-of-sight deposition of a large fraction of low-energy sputtered atoms onto neighboring asperities [12]. In addition, there is a small decrease at $\theta > 85°$ for different $\sigma$, as shown in figure 3(*b*)), which is caused by increased ion backscattering at glancing $\theta$.

Thus, low-roughness surfaces under ion irradiation with large incident polar angles and high-roughness surfaces under ion irradiation with small incident polar angles exhibit dramatically reduced ion implantation and sputtering of W, respectively. At 400 °C –800 °C in ITER [8], implanted D/T/He atoms will diffuse quickly, some of which would desorb from the surface, while the other portion would be trapped by the enhanced interfacial area of the nanostructured surface [63]. It is a very complex dynamic process for the retention

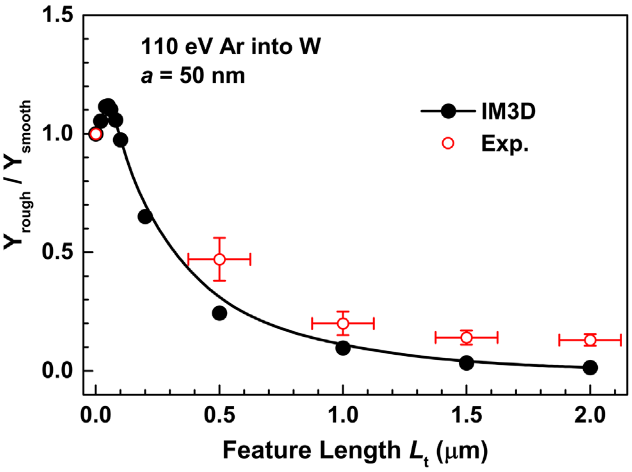

**Figure 7.** Comparison of IM3D-calculated sputtering yields $Y_{\mathrm{rough}}/Y_{\mathrm{smooth}}$ with experimental results [12], for 110 eV Ar-ion sputtering of W rough surfaces with $a = 50$ nm and feature length $L_t$ ranging from 0–2 $\mu$m. A spline fitting line is also drawn to guide the reader's eye.

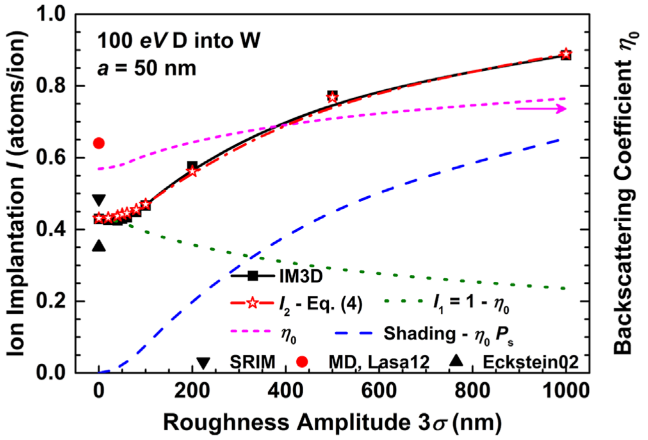

**Figure 8.** The D-ion implantation $I$ calculated by IM3D and estimated by equation (4) using $3\sigma = 0$–$1000$ nm for W rough surface with $a = 50$ nm. 100 eV D-ion beam with random normal incidence is applied here. The SRIM (calculated by SRIM-2013 [32] with default settings), TRIM.SP [42] and MD [48] values of D-ion implantation for a smooth surface are also given for comparison.

of implanted ions in W in view of the simultaneous effects of ion implantation, diffusion and trapping at finite temperature and longer timescales. Moreover, the high surface area may further aggravate implanted-atom desorption. In fact, we have previously systematically investigated He [64, 65] and D [66, 67] retention behaviors in smooth surface W by combining binary collision and cluster dynamics models. When the major contribution of diffusion and trapping to atom desorption is fixed, ion implantation would be the only key factor left to affect the retention of these species.

Finally, the reliability of IM3D's predictions is evaluated by comparing them to existing experiments. As shown in figure 7, the sputtering yield of rough W ($3\sigma$ from 0–2 $\mu$m) under 110 eV of Ar-ion irradiation given by IM3D agrees well for small feature lengths $L_t$ to that of fuzzy W by mass loss measurements, while larger features show less agreement. The sputtering yield of 0.046 atoms/ion was obtained for the smooth W surface, which agrees well with the TRIM.SP calculation [42] and measurements from ion beams [59] and plasma ($0.05 \pm 0.002$) [12]. The $Y_{\mathrm{rough}}/Y_{\mathrm{smooth}}$ ratio decreases with the increasing feature length $L_t$, which agrees with experiments [12] when taking $a = 50$ nm. In the experiment $L_t$ denotes the fuzzy layer thickness measured from SEM cross sections or estimated from the surface temperature and the plasma exposure time by a $t^{1/2}$ dependence; in the simulation meanwhile, it is selected as the roughness amplitude $3\sigma$ which is on the same level of the measured layer thickness. Nishijima *et al* pointed out that this trend is consistent with the change in the complementary fuzz porosity [12]. Because the fuzz porosity is a characteristic parameter of surface morphology and increases with $L_t$, it should thus have a similar trend with surface roughness amplitude. IM3D values are a little lower than those of the experiment; this might be due to the simplicity of its rough surface model and the underestimation of the rough peak interval $a$ and the feature length $L_t$ (~$3\sigma$). While it is difficult to determine an exact value of the experimental peak interval for different fuzzy structures, setting $a$ to 50 nm should be physically reasonable, since the feature size of fuzzy structures is usually in the range of 10s of nm [37].

### *3.4. Connecting smooth-surface results with rough-surface results*

In order to describe the analytical relationship of $I$ versus $\sigma$ (the shading effect), a simple formula is proposed at normal incidence; this is indicated by the black solid line in figures 8 and 9(*a*). As shown in figures 1(*b*) and (*d*), the slope angle $\alpha$ of a surface facet can be defined as $\alpha \equiv \arctan(\Delta Z/a)$, where $\Delta Z$ is the profile element height (the sum of the height of the peak and depth of the valley of a triangular element). The mean value of the slope angles, $\bar{\alpha}$, can be estimated by averaging with the Gaussian distribution for the rough surfaces with $3\sigma = 0$–$1000$ nm and $a = 50$ nm, as shown in SOM 2. As shown in figure 1(*d*), the effective incident angle of normal-incidence ($\theta = 0$) ions is approximately equal to $\alpha$. Thus, to a zeroth-order approximation (only taking into account the backscattering effect related to $\bar{\alpha}$ but not the shading effect due to rough peaks), the ion implantation is defined as (green dotted line in figures 8 and 9(*a*)),

$$I_0(\bar{\alpha}) \equiv 1 - \eta_0(\bar{\alpha}), \tag{2}$$

where $\eta_0(\bar{\alpha})$ is the flat-surface backscattering coefficient as a function of the mean effective incident angle (also equal to $\bar{\alpha}$ as defined in SOM 2), which was calculated by IM3D directly for an infinite, smooth surface (magenta, short dashed lines in figures 8 and 9(*a*)).

In fact, a fraction of backscattered ions would be shaded by surface asperities. Only backscattered ions exiting within a critical polar angle range $\theta' < (90° - \bar{\alpha}) + \arctan[(2a - Z \cdot \tan(90° - \bar{\alpha}))/Z]$ could be shaded, as discussed in SOM 3. The emission probability or the complementary shading probability ($P_s$) are thus estimated by numerically integrating the exact angular distribution of outgoing ions

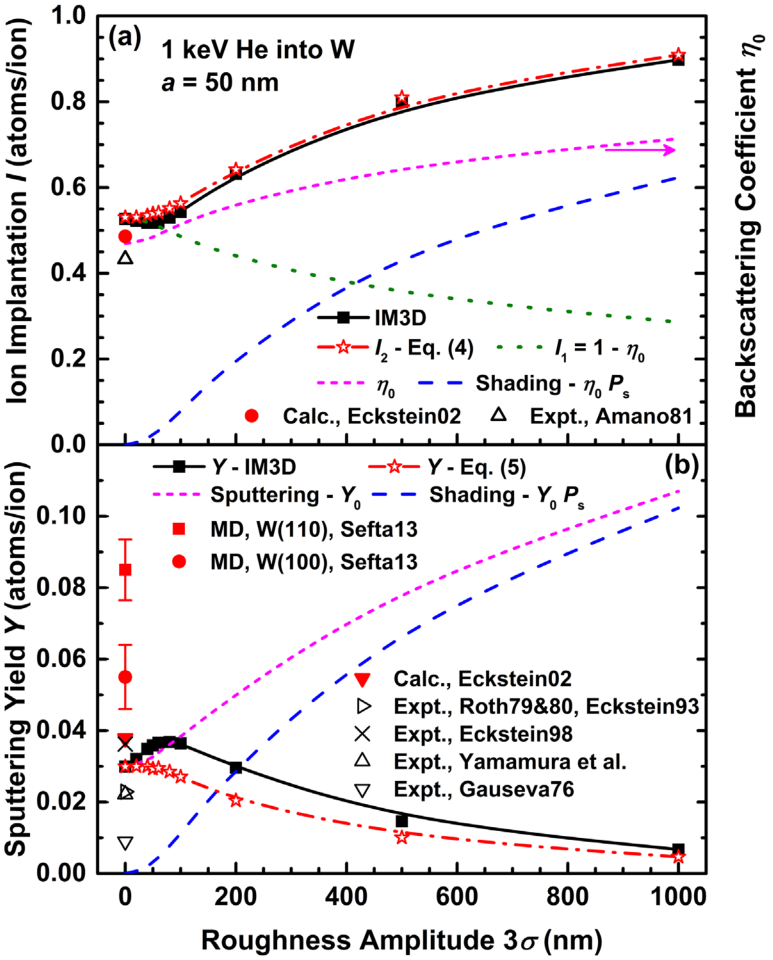

**Figure 9.** (*a*) The He-ion implantation $I$ calculated by IM3D and estimated by equation (4), as well as (*b*) the sputtering yield $Y$ calculated by IM3D and estimated by equation (5), along with $3\sigma$ from 0–1000 nm for rough W with $a = 50$ nm. 1 keV He-ion beam with random normal incidence is applied here. The TRIM.SP [42] and experimental values [49] of He-ion implantation $I_0$ as well as the TRIM.SP [42], MD [46, 50] and experimental values [51–58] of He sputtering yields $Y_0$ for a smooth surface are also given for comparison.

within the emission solid angle, and from zero to the mean profile element height $\overline{\Delta Z}$ of rough peaks, as shown in figures 8 and 9(*a*) (blue dashed line) and discussed in SOM 3. The angular distribution of backscattered ions/sputtered atoms is anisotropic related to the incident energies and directions of ions, as shown in [12, 44, 45] and in SOM 3 has been already included in the estimation of $P_s$ automatically. Therefore, if we suppose that all the shaded ions are deposited in asperities as a first-order approximation, the ion implantation can be described by,

$$I_1 = 1 - \eta_0(\overline{\alpha}) + \eta_0(\overline{\alpha}) \cdot P_s. \tag{3}$$

If we consider that there is still some probability for the shaded ions to escape from asperities, a more accurate estimation of the ion implantation in the rough surface can be given by a second-order approximation,

$$I_2 = 1 - \eta_0(\overline{\alpha}) + I_2^0 \cdot \eta_0(\overline{\alpha}) \cdot P_s. \tag{4}$$

Here, the secondary implantation $I_2^0 = 1 - \eta_0(\overline{\alpha}) + I_1 \cdot \eta_0(\overline{\alpha}) \cdot P_s$ ($I_1$ is used as an initial guess), as $I_2^0$ should be smaller than $I_1$ due to the lower energies and shading probability of secondary ions. In fact, this approximation is more reasonable for large $\sigma$, as discussed in SOM 4.

As shown in figures 8 and 9(*a*), a good agreement has been reached between the IM3D results (black solid line) and the estimations made by equation (4) (red line), which illustrates that the relationship proposed here is quite robust. Under the critical roughness amplitude of $3\sigma = 50$ nm, the backscattering effect $\eta_0(\overline{\alpha})$ dominates the primary ion implantation in W. The shading effect appears after $3\sigma > 50$ nm, and becomes more important to ion implantation in W with increasing $3\sigma$. The interplay between these two effects changes the ion implantation in rough W. The small deviation between the calculated and analytical results mainly comes from the estimation of $I_2$ when employing $I_2^0$ for lower-energy secondary backscattered ions, as discussed in SOM 4.

Similarly, the relationship of $Y$ versus $\sigma$ can also be described by a simple analytical expression, by taking into account the shading ($P_s$) of primary sputtered W atoms by surface asperities,

$$Y = A(\overline{\alpha}) \cdot Y_0(\overline{\alpha}) \cdot (1 - P_s), \tag{5}$$

where $Y_0(\overline{\alpha})$ is the $\overline{\alpha}$-dependent sputtering yield of the smooth surface, as shown in figure 3(*b*). $A(\overline{\alpha})$ is an $\overline{\alpha}$-dependent coefficient relating the secondary sputtering to reflected He ions or sputtered W atoms, which would increase with increasing $Y_0(\overline{\alpha})$ and reach a saturation value quickly. $A(\overline{\alpha})$ is much complicated for random rough surfaces, but saturates quickly due to the shading rate approaching unity at high $\sigma$, as discussed in SOM 4. For simplicity, we neglect the secondary sputtering effect here and set $A(\overline{\alpha}) = 1$, as the emitted atoms could induce less serious secondary surface sputtering when their mean energy is close to/under the threshold energy that can cause W sputtering. In figure 9(*b*), a consistent trend between IM3D and equation (5) is obtained except for an underestimation of values due to the exclusion of secondary sputtering in the analytical expression. In fact, the secondary sputtering effect will induce about 45% extra sputtered atoms for rough W under 1 keV He-ion irradiation, as shown in SOM 4.

## 4. Summary and discussions

Ion implantation can be enhanced by a factor of two with rough surfaces compared to smooth surfaces depending on the roughness amplitude, while the sputtering yield of the rough surface is around one order of magnitude lower than that of the smooth surface due to recapture by adjacent peaks. This enhancement of ion absorption (the enhancement of ion implantation and the reduction of ion sputtering) due to surface roughness, called the ion radiation albedo effect or “ion sponge” effect, is mainly determined by the nano-geometric shading process and is less dependent on the type and energy of incident ions. In addition, according to the proposed simple analytical formulas (equations (4) and (5)), one can more clearly understand the contributing factors to ion implantation and sputtering for different rough surfaces or even other types of nano-arrays. Ion implantation and sputtering yields of a typical rough surface can also be estimated by providing only the incident and emission angle-dependent ion backscattering coefficient and the sputtering yield of the smooth surface, respectively, instead of constructing a complex surface model. Furthermore, for both smooth and rough surfaces, increasing the angle of incidence further increases ion backscattering and sputtering (except for a small decrease in sputtering at the glancing incidence).

In general, in fusion engineering the radiation albedo effect could be deleterious as it enhances ion implantation (even though they may be more easily desorbed later due to larger surface area to volume ratio), but is beneficial as it reduces ion sputtering for PFMs like W. Moreover, this effect could be beneficial in other contexts, for example ion-beam processing of surfaces to induce high surface area and light absorption, such as in photoelectrochemical water splitting, solar energy conversion, and pyroelectric detectors [2, 68–70].

## Acknowledgments

This work was supported by the National Natural Science Foundation of China under Grant Nos. 11275229, 11475215 & NSAF U1230202, the key project of the National Science Foundation of China under Grant No. 11534012, the Special Funds for the Major State Basic Research Project of China (973) under Grant No. 2012CB933702, the Youth Innovation Promotion Association of CAS under Grant No. 2016386, and the Director Grants of CASHIPS. Part of the calculations were performed at the Center for Computational Science at CASHIPS, the ScGrid of the Supercomputing Center, and the Computer Network Information Center of the Chinese Academy of Sciences. J.L. and Y.Y. acknowledge support from NSF DMR-1410636 and DMR-1120901. M.P.S. acknowledges support from the U.S. Nuclear Regulatory Commission (NRC), under grant number NRC-HQ-84-15-G-0045. Computational time on the Extreme Science and Engineering Discovery Environment (XSEDE) under grant number TG-DMR130038 is gratefully acknowledged. Z.D. acknowledges support from the National Natural Science Foundation of China (Nos 11274288 & 11574289), the Ministry of Education of China (No. 20123402110034) and the ‘111’ project (No. B07033).

## References

[1] Krasheninnikov A.V. and Nordlund K. 2010 Ion and electron irradiation-induced effects in nanostructured materials *J. Appl. Phys.* **107** 071301

[2] Tanyeli I., Marot L., Mathys D., van de Sanden M.C. and De Temmerman G. 2015 Surface modifications induced by high fluxes of low energy helium ions *Sci. Rep.* **5** 9779

[3] Krauz V.I., Martynenko Y.V., Svechnikov N.Y., Smirnov V.P., Stankevich V.G. and Khimchenko L.N. 2011 Nanostructures in controlled thermonuclear fusion devices *Phys.-Usp.* **53** 1015–38

[4] Dhara S. 2007 Formation, dynamics, and characterization of nanostructures by ion beam irradiation *Crit. Rev. Solid State Mater. Sci.* **32** 1–50

[5] Federici G. *et al* 2001 Plasma-material interactions in current tokamaks and their implications for next step fusion reactors *Nucl. Fusion* **41** 1967–2137

[6] Roth J. *et al* 2009 Recent analysis of key plasma wall interactions issues for ITER *J. Nucl. Mater.* **390–1** 1–9

[7] Nordlund K., Björkas C., Ahlgren T., Lasa A. and Sand A.E. 2014 Multiscale modelling of plasma–wall interactions in fusion reactor conditions *J. Phys. D: Appl. Phys.* **47** 224018

[8] Wirth B.D., Hammond K.D., Krasheninnikov S.I. and Maroudas D. 2015 Challenges and opportunities of modeling plasma–surface interactions in tungsten using high-performance computing *J. Nucl. Mater.* **463** 30–8

[9] Kajita S., Sakaguchi W., Ohno N., Yoshida N. and Saeki T. 2009 Formation process of tungsten nanostructure by the exposure to helium plasma under fusion relevant plasma conditions *Nucl. Fusion* **49** 095005

[10] Sandoval L., Perez D., Uberuaga B.P. and Voter A.F. 2015 Competing kinetics and He bubble morphology in W *Phys. Rev. Lett.* **114** 105502

[11] Lasa A., Tähtinen S.K. and Nordlund K. 2014 Loop punching and bubble rupture causing surface roughening—a model for W fuzz growth *Europhys. Lett.* **105** 25002

[12] Nishijima D., Baldwin M.J., Doerner R.P. and Yu J.H. 2011 Sputtering properties of tungsten ‘fuzzy’ surfaces *J. Nucl. Mater.* **415** S96–9

[13] Frost F., Ziberi B., Schindler A. and Rauschenbach B. 2008 Surface engineering with ion beams: from self-organized nanostructures to ultra-smooth surfaces *Appl. Phys.* A **91** 551–9

[14] Kajita S., Saeki T., Yoshida N., Ohno N. and Iwamae A. 2010 Nanostructured black metal: novel fabrication method by use of self-growing helium bubbles *Appl. Phys. Exp.* **3** 085204

[15] El-Atwani O., Gonderman S., Efe M., Gregory D.T., Morgan T., Bystrov K., Klenosky D., Qiu T. and Allain J.P. 2014 Ultrafine tungsten as a plasma-facing component in fusion devices: effect of high flux, high fluence low energy helium irradiation *Nucl. Fusion* **54** 083013

[16] ‘t Hoen M.H.J., Balden M., Manhard A., Mayer M., Elgeti S., Kleyn A.W. and Zeijlmans van Emmichoven P.A. 2014 Surface morphology and deuterium retention of tungsten after low- and high-flux deuterium plasma exposure *Nucl. Fusion* **54** 083014

[17] Wei Q., Eddy M., Li K.D. and Wang L. 2009 Influence of surface morphology on sputtering yields *J. Phys. D: Appl. Phys.* **42** 165304

[18] Doerner R.P., Björkas C., Nishijima D. and Schwarz-Selinger T. 2013 Erosion of beryllium under high-flux plasma impact *J. Nucl. Mater.* **438** S272–5

[19] Doerner R.P., Nishijima D. and Schwarz-Selinger T. 2014 Impact of surface morphology on sputtering during high-fluence plasma exposure *Phys. Scr.* **T159** 014040

[20] Doerner R.P., Nishijima D. and Schwarz-Selinger T. 2012 Measuring the difference between gross and net erosion *Nucl. Fusion* **52** 103003

[21] Doerner R.P., Jepu I., Nishijima D., Safi E., Bukonte L., Lasa A., Nordlund K. and Schwarz-Selinger T. 2015 The relationship between gross and net erosion of beryllium at elevated temperature *J. Nucl. Mater.* **463** 777–80

[22] Ogorodnikova O.V., Roth J. and Mayer M. 2008 Ion-driven deuterium retention in tungsten *J. Appl. Phys.* **103** 034902

[23] Alimov V.K. and Roth J. 2007 Hydrogen isotope retention in plasma-facing materials: review of recent experimental results *Phys. Scr.* **T128** 6–13

[24] Bizyukov I., Krieger K., Lee H., Schmid K., Haasz A.A. and Davis J.W. 2012 An overview of sputtering-related processes occurring at mixed surfaces formed by simultaneous $C^+$ and $D^+$ irradiation of W *J. Nucl. Mater.* **427** 401–10

[25] Gonzalez-Arrabal R., Panizo-Laiz M., Gordillo N., Tejado E., Munnik F., Rivera A. and Perlado J.M. 2014 Hydrogen accumulation in nanostructured as compared to the coarse-grained tungsten *J. Nucl. Mater.* **453** 287–95

[26] Sigmund P. 1969 Theory of sputtering. I. Sputtering yield of amorphous and polycrystalline targets *Phys. Rev.* **184** 383–416

[27] Kustner M., Eckstein W., Hechtl E. and Roth J. 1999 Angular dependence of the sputtering yield of rough beryllium surfaces *J. Nucl. Mater.* **265** 22–7

[28] Molodtsov S.L., Gurbich A.F. and Jeynes C. 2008 Accurate ion beam analysis in the presence of surface roughness *J. Phys. D: Appl. Phys.* **41** 205303

[29] Ruzic D.N. 1990 The effects of surface roughness characterized by fractal geometry on sputtering *Nucl. Instrum. Methods Phys. Res.* B **47** 118–25

[30] Kenmotsu T., Yamamura Y., Muramoto T. and Hirotani N. 2005 Simulation studies on sputtering in rough surface *Nucl. Instrum. Methods Phys. Res.* B **228** 369–72

[31] Hu A. and Hassanein A. 2012 How surface roughness affects the angular dependence of the sputtering yield *Nucl. Instrum. Methods Phys. Res.* B **281** 15–20

[32] Ziegler J.F., Ziegler M.D. and Biersack J.P. 2010 SRIM—The stopping and range of ions in matter. *Nucl. Instrum. Methods Phys. Res.* B **268** 1818–23

[33] Li Y.G., Yang Y., Short M.P., Ding Z.J., Zeng Z. and Li J. 2015 IM3D: a parallel Monte Carlo code for efficient simulations of primary radiation displacements and damage in 3D geometry *Sci. Rep.* **5** 18130

[34] Li Y.G., Mao S.F., Li H.M., Xiao S.M. and Ding Z.J. 2008 Monte Carlo simulation study of scanning electron microscopy images of rough surfaces *J. Appl. Phys.* **104** 064901

[35] Kinchin G.H. and Pease R.S. 1955 The displacement of atoms in solids by radiation *Rep. Prog. Phys.* **18** 1–51

[36] Norgett M.J., Robinson M.T. and Torrens I.M. 1975 A proposed method of calculating displacement dose rates *Nucl. Eng. Des.* **33** 50–4

[37] Fiflis P., Curreli D. and Ruzic D.N. 2015 Direct time-resolved observation of tungsten nanostructured growth due to helium plasma exposure *Nucl. Fusion* **55** 033020

[38] Li H.M. and Ding Z.J. 2005 Monte Carlo simulation of secondary electron and backscattered electron images in scanning electron microscopy for specimen with complex geometric structure *Scanning* **27** 254–67

[39] Li Y.G., Ding Z.J. and Zhang Z.M. 2009 Monte Carlo simulation study of scanning Auger electron images *J. Appl. Phys.* **106** 024316

[40] Zhang P., Wang H.Y., Li Y.G., Mao S.F. and Ding Z.J. 2012 Monte Carlo simulation of secondary electron images for real sample structures in scanning electron microscopy *Scanning* **34** 145–50

[41] Da B., Mao S.F., Zhang G.H., Wang X.P. and Ding Z.J. 2012 Monte Carlo modeling of surface excitation in reflection electron energy loss spectroscopy spectrum for rough surfaces *J. Appl. Phys.* **112** 034310

[42] Eckstein W. 2002 *Calculated Sputtering, Reflection and Range Values* (IPP 9/132) (Garching: Max-Planck-Institute für Plasmaphysik)

[43] Eckstein W. 2009 *Reflection (Backscattering)* (IPP 17/12) (Garching: Max-Planck-Institute für Plasmaphysik)

[44] Borovikov V., Voter A.F. and Tang X.Z. 2014 Reflection and implantation of low energy helium with tungsten surfaces *J. Nucl. Mater.* **447** 254–70

[45] Hofsäss H., Zhang K. and Mutzke A. 2014 Simulation of ion beam sputtering with SDTrimSP, TRIDYN and SRIM *Appl. Surf. Sci.* **310** 134–41

[46] Ferroni F., Hammond K.D. and Wirth B.D. 2015 Sputtering yields of pure and helium-implanted tungsten under fusion-relevant conditions calculated using molecular dynamics *J. Nucl. Mater.* **458** 419–24

[47] Hofsäss H., Bobes O. and Zhang K. 2013 Is sputtering relevant for ion-induced self-organized pattern formation? *AIP Conf. Proc.* **1525** 386–91

[48] Lasa A., Björkas C., Vörtler K. and Nordlund K. 2012 MD simulations of low energy deuterium irradiation on W, WC and surfaces *J. Nucl. Mater.* **429** 284–92

[49] Amano J. and Seidman D.N. 1981 Experimental determination of the particle reflection coefficients of low-energy (100–1500 eV) $^3$He and $^4$He atoms from the (1 1 0) plane of tungsten *J. Appl. Phys.* **52** 6934

[50] Sefta F., Juslin N., Hammond K.D. and Wirth B.D. 2013 Molecular dynamics simulations on the effect of sub-surface helium bubbles on the sputtering yield of tungsten *J. Nucl. Mater.* **438** S493–6

[51] Roth J., Bohdansky J. and Ottenberger W. 1979 *Data on Low Energy Light Ion Sputtering* (*IPP 9/26*) (Garching: Max-Planck-Institute für Plasmaphysik)

[52] Roth J., Bohdansky J. and Martinelli A.P. 1980 Low energy light ion sputtering of materials and carbides *Radiat. Eff.* **48** 213–9

[53] Eckstein W., Garcia-Rosales C., Roth J. and Ottenberger W. 1993 *Sputtering Data* (*IPP 9/82*) (Garching: Max-Planck-Institute für Plasmaphysik)

[54] Eckstein W. 1998 *Sputtering, Reflection and Range Values for Plasma Edge Codes* (*IPP 9/117*) (Garching: Max-Planck-Institute für Plasmaphysik)

[55] Yamamura Y. and Tawara H. 1995 Energy dependence of ion-induced sputtering yields from monoatomic solids at normal incidence *Report* NIFS-DATA-23

[56] Yamamura Y., Sakaoka K. and Tawara H. 1995 Computer simulation and data compilation of sputtering yields by hydrogen isotopes ($^1$H+, $^2$D+, $^3$T+) and helium ($^4$He+) ion impact from monoatomic solids at normal incidence *Report* NIFS-DATA-31

[57] Yamamura Y. and Tawara H. 1996 Energy dependence of ion-induced sputtering yields from monoatomic solids at normal incidence *Atom. Data Nucl. Data Tab.* **62** 149–253

[58] Gauseva M.I. and Martynenko Y.V. 1976 *Fiz. Plaz.* **2** 593

[59] Eckstein W. 2007 *Sputtering Yields. Sputtering by Particle Bombardments* ed R. Behrisch and W. Eckstein (Berlin: Springer)

[60] Stoller R.E., Toloczko M.B., Was G.S., Certain A.G., Dwaraknath S. and Garner F.A. 2013 On the use of SRIM for computing radiation damage exposure *Nucl. Instrum. Methods Phys. Res.* B **310** 75–80

[61] Sugiyama K., Schmid K. and Jacob W. 2016 Sputtering of iron, chromium and tungsten by energetic deuterium ion bombardment *Nucl. Mater. Energy* **8** 1–7

[62] Eckstein W., Verbeek H. and Biersack J.P. 1980 Computer simulation of the backscattering and implantation of hydrogen and helium *J. Appl. Phys.* **51** 1194–200

[63] Ackland G. 2010 Controlling radiation damage *Science* **327** 1587–8

[64] Li Y.G., Zhou W.H., Ning R.H., Huang L.F., Zeng Z. and Ju X. 2012 A cluster dynamics model for accumulation of helium in tungsten under helium ions and neutron irradiation *Commun. Comput. Phys.* **11** 1547–68

[65] Li Y.G., Zhou W.H., Huang L.F., Zeng Z. and Ju X. 2012 Cluster dynamics modeling of accumulation and diffusion of helium in neutron irradiated tungsten *J. Nucl. Mater.* **431** 26–32

[66] Ning R.H., Li Y.G., Zhou W.H., Zeng Z. and Xin J. 2012 An improved cluster dynamics model for hydrogen retention in tungsten *Int. J. Mod. Phys.* C **23** 1250042

[67] Ning R.H., Li Y.G., Zhou W.H., Zeng Z. and Ju X. 2012 Modeling D retention in W under D ions and neutrons irradiation *J. Nucl. Mater.* **430** 20–6

[68] de Respinis M., De Temmerman G., Tanyeli I., van de Sanden M.C.M., Doerner R.P., Baldwin M.J. and van de Krol R. 2013 Efficient plasma route to nanostructure materials: case study on the use of m-WO3 for solar water splitting *ACS Appl. Mater. Interfaces* **5** 7621–5

[69] Brown R.J.C., Brewer P.J. and Milton M.J.T. 2002 The physical and chemical properties of electroless nickel-phosphorus alloys and low reflectance nickel-phosphorus black surfaces *J. Mater. Chem.* **12** 2749–54

[70] Yang Z.P., Ci L.J., Bur J.A., Lin S.Y. and Ajayan P.M. 2008 Experimental observation of an extremely dark material made by a low-density nanotube array *Nano. Lett.* **8** 446–51

# Supplementary Materials

## S1. The nano-energetic and nano-geometric effects

As the size of nano-features becomes comparable to the sizes of the collision cascade or sub-cascades, the high surface-to-volume ratio of nanostructured materials induce two new effects, which we call the nano-energetic effect and nano-geometric effect. Due to quantum confinement, surface stress and elastic interactions, fundamental material energetics such as electronic stopping power and displacement energy ($E_d$) could change with the size reduction, which causes the nano-energetic (N-E) effect. Meanwhile, the nano-geometric (N-G) effect will also influence the trajectory of an ion when it moves through different material zones, in processes such as trajectory emission, re-entry, sputtering, and shading [1].

Here we estimate the exact roles of these two effects on primary radiation damage in nanostructures. A regular column is used as a typical model for a class of nanostructured materials, such as nanowires, nanoporous structures, and “fuzz” [2-4]. Thus, a typical columnar nano-system constructed by the Constructive Solid Geometry (CSG) algorithm in IM3D is selected here. The vacancy depth-distribution in a gold column target under normally incident, 45 keV Ne-ion implantation is shown in figure S1. Due to the N-G effect, the range of vacancy depth-distributions (figure S1(a)) and the total number of vacancies (figure S1(b)) both increase with increasing column diameters, and finally approach the bulk value after a critical diameter of around 200 nm. When the column size is smaller than a critical value $L_C$, the N-E effect can contribute up to 50% of defect production (figure S1(c)), which should not be neglected. Here, $L_C$ has a value of about 20 nm, as it is known that the thermodynamic properties change less sensitively with object sizes above 20 nm [5].

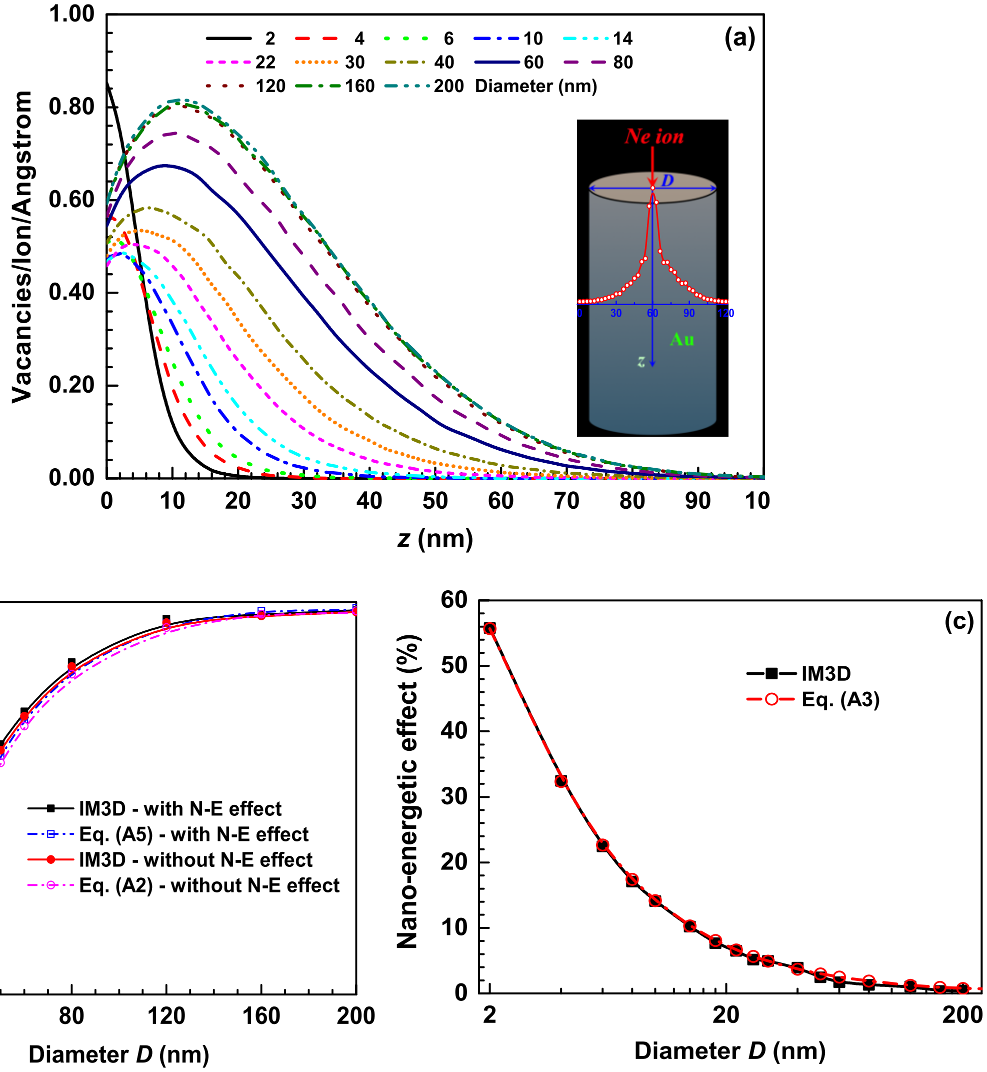

**Figure S1.** (a) The depth-distributions and (b) total number of vacancies calculated by IM3D and fitted by equation (A2) and (A5), as well as (c) the contribution of the N-E effect to the total number of vacancies, for a gold nanowire with different diameters under 45 keV Ne-ion irradiation with a centered, normally-incident beam. The inserted figure in (a) shows the radial distribution of vacancies in Au bulk.

Assume that the radial distribution of radiation defects such as vacancies, $N(r)$, produced by an ion in a semi-infinite bulk target follows an exponential decay (as shown by the inserted figure in figure S1(a)),

$$N(r) = N_0 e^{-r/t},\ r \in [0,\ \infty), \qquad \text{(A1)}$$

where, $N_0$ is the number of defects at $r = 0$ and $t$ is the effective attenuation length of defects in radial direction (here chosen as 12.5 nm). The amount of defects in this nanowire can be obtained by integrating equation (A1) over the volume of the symmetric column (see figure S1(a)),

$$N_{\mathrm{d}}\left(R\right) = \int_0^R \int_0^{2p} N\left(r\right) \cdot r\,dr\,dq = 2pN_0t^2 \cdot \left[1 - \left(1 + R/t\right) \cdot e^{-R/t}\right] = N_d^0 \cdot \left[1 - \left(1 + R/t\right) \cdot e^{-R/t}\right], \quad \text{(A2)}$$

where $R$ is the radius of the column, and $N_d^0 = 2pN_0t^2$ is the defect concentration in the bulk. Equation (A2) can describe the total amount of vacancies calculated by IM3D when the diameter ($D = 2R$) of the column is larger than $L_{\mathrm{C}}$, as shown in figure S1(b). Moreover, this integration method can also be extended to consider the N-G effect in convex, arbitrarily complex nanostructures by numerical integration along their whole volume.

However, as the column diameter becomes smaller than $L_{\mathrm{C}}$, the N-E effect appears and becomes more and more important with decreasing diameter [5], as shown in figure S1(c). Assuming that the displacement and binding energies follow a universal relationship to the thermodynamic properties of the material (such as cohesive energy, vacancy formation energy, or diffusion activation energy) along with the diameter $D$ of the nanostructure, we define the strength of the N-E effect as [6-8],

$$\frac{E\left(R\right)}{E\left(\infty\right)} = \left(1 - \frac{1}{2D/h - 1}\right)\exp\left(-\frac{2S_{\mathrm{b}}}{3R_{\mathrm{c}}}\frac{1}{2D/h - 1}\right), \quad \text{(A3)}$$

where $S_{\mathrm{b}}$ is the bulk solid-vapor transition entropy (106.8 J mol$^{-1}$ K$^{-1}$ for Au [7]), $R_{\mathrm{c}}$ is the ideal gas constant, and $h$ is the nearest inter-atomic spacing (0.288 nm for Au [7]). Primary defect production will therefore be inversely proportional to the column size. Furthermore, the N-E effect can also affect the electronic energy loss during ion transport in nanostructured materials. The electronic energy loss is defined to be proportional to the transport trajectory length $l$ (valid at least for any case but ultrathin solid targets [9]), the atomic density $n$ and the scattering cross-section $\sigma_{\mathrm{e}}$ [10],

$$E_{\mathrm{e}} = \left(\frac{dE}{dx}\right)_{\mathrm{e}} = l \cdot n \cdot \sigma_{\mathrm{e}}\,. \quad \text{(A4)}$$

The change of energy loss caused by the N-E effect only comes from the contribution of the density change of nanostructured materials. This is because the scattering cross-section is only a single atom property under binary collision approximation (BCA), and the transport trajectory length is not an intrinsic material property. The influence of the N-E effect on density changes is much complex with no universal relationship, which may increase or decrease with decreasing nanostructure size [6, 11]. Fortunately, the effect of size on the density can be neglected due to the change of the nearest inter-atomic spacing $h$ being only 0.1-3% when $R < 10$ nm (or $D < 20$ nm) [6, 12]. Hence, in IM3D, we can estimate the N-E effect on defect production by just adjusting the threshold energies with equation (A3). The revised IM3D results of total vacancy number with the diameter of nanostructures are given in figure S1(b). Due to the N-E effect, the number of vacancies is higher (up to 50%) than that of only taking account of the N-G effect, especially when the size of the structures declines (figure S1(c)).

In order to analyze the respective contributions from the N-E effect and N-G effect, we modify the well-known Norgett-Robinson-Torrens (NRT) model ( $N_{\mathrm{NRT}} = 0.8E_{\mathrm{v}}/2E_{\mathrm{d}}$ , an inverse proportion between the defect production and the displacement energy $E_{\mathrm{d}}$ for $E_{\mathrm{v}} \geq 2E_{\mathrm{d}}/0.8$, where $E_{\mathrm{v}}$ is the energy which goes into nuclear collisions) [13, 14] to simply estimate the defect production as,

$$\frac{N_{\mathrm{D}}(R)}{N_D^0} = \frac{E_{\mathrm{d}}(\infty)}{E_{\mathrm{d}}(R)} \cdot \frac{N_{\mathrm{d}}(R)}{N_{\mathrm{d}}^0} = \left(1 + \frac{1}{4R/h - 2}\right) \exp\left(\frac{2S_{\mathrm{b}}}{3R_{\mathrm{c}}} \frac{1}{4R/h - 1}\right) \cdot \left[1 - \left(1 + R/t\right) \cdot e^{-R/t}\right]. \quad \text{(A5)}$$

where $N_{\mathrm{D}}(R)$ and $N_D^0$ are the defect production terms in a column with radius $R$ and in the bulk, respectively.

The vacancy production calculated by equation (A5) is also shown in figure S1(b). The proposed analytical estimations better describe the calculated vacancy-diameter relation. In particular, the contribution of the N-E effect to the total amount of vacancies estimated by IM3D and equation (A5) is nearly the same (figure S1 (c)). It thus directly illustrates that the N-E and N-G effect are the main factors to the distributions of primary radiation damage in nanostructured materials. The relative deviation between IM3D results and equations ((A2) and (A5)) is considerable, especially in the size-range of $D <$

40 nm, which should mainly come from the inability of the exponential decay (equation (A1)) to fit the relationship of the radial distribution of vacancies exactly, especially when $r$ is small. In IM3D, we can consider the bulk energetic parameters to be valid when the target size is larger than $L_C$. For objects smaller than $L_C$, IM3D can use a set of modified parameters to account for the N-E effect.

Fortunately, the typical feature size of roughness peaks or fuzzy structures in metals under low energy ion irradiation is in the range of 10's of nm (50 nm is used in our model). Thus, the N-E effect can be reasonably neglected, as also shown by the good agreement between IM3D simulations, and analytical and experimental results (figures 8 and 9 in the main text). Thus, we just highlight the important role of N-G effect on the ion radiation albedo effect.

## S2. Surface texture parameters in a Gaussian-type rough surface profile

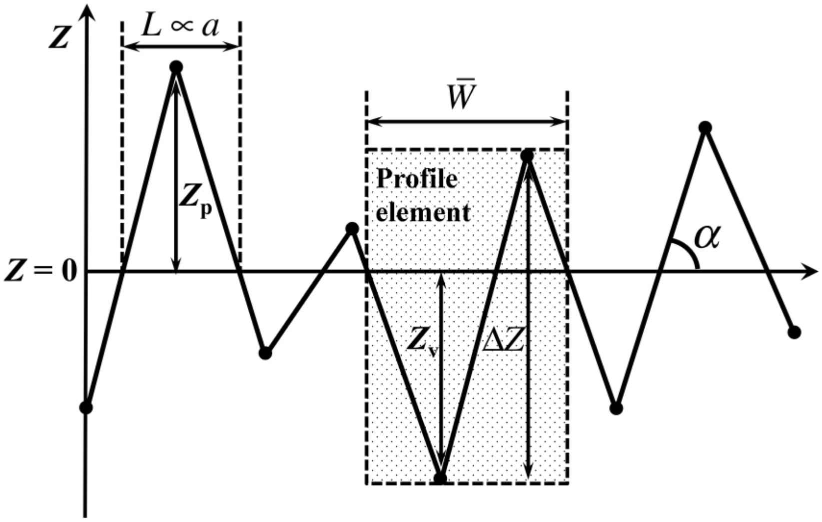

**Figure S2.** Schematic of the surface texture parameters in a Gaussian-type rough surface profile.

The Gaussian-type rough surface proposed here is a simple and typical surface texture according to the definition in ISO 4287 [15]. ISO 4287 specifies terms, definitions and parameters for the determination of surface texture (roughness, waviness, and primary profile) by profiling methods, where the surface profile results from the intersection of the real surface by a specified plane. The surface texture parameters of Gaussian-type rough surface profile can thus be given as following (figure S2). The measured mean line for the roughness profile is at $Z = 0$, the material length of profile $L$ at level $Z = 0$ is proportional to $a$, both the maximum profile peak height $Z_\mathrm{p}$ and maximum profile valley depth $Z_\mathrm{v}$ are equal to $3\sigma$, and the mean width of profile element $\bar{W}$ is about $2a$. In particular, the profile element height $\Delta Z\left(\geq 0\right)$ (sum of the height of the peak and depth of the valley of a rough profile element) also follows the truncated Gaussian distribution,

$$F\left(\Delta Z\right) \propto \exp\left(-\Delta Z^2/2\sigma'^2\right), \quad \Delta Z \in \left[0, 3\sqrt{2}\sigma'\right], \tag{A6}$$

where $\sigma' \approx \sqrt{2}\sigma$, for $\left\langle\left(Z_1^2 - Z_2^2\right)\right\rangle \approx 2\sigma^2$.

The mean local slope angle of rough surface (or the mean effective incident angle of ions), $\bar{\alpha}$, can thus be determined as,

$$\begin{aligned} \bar{\alpha} &= \frac{\int_0^{3\sqrt{2}\sigma'} \alpha F\left(\Delta Z\right) d\Delta Z}{\int_0^{3\sqrt{2}\sigma'} F\left(\Delta Z\right) d\Delta Z} = \frac{\int_0^{3\sqrt{2}\sigma'} \arctan(\Delta Z/a) \cdot \exp\left(-\Delta Z^2/2\sigma'^2\right) d\Delta Z}{\int_0^{3\sqrt{2}\sigma'} \exp\left(-\Delta Z^2/2\sigma'^2\right) d\Delta Z} \\ &= \frac{1}{\sigma'} \int_0^{3\sqrt{2}\sigma'} \arctan(\Delta Z/a) \cdot \exp\left(-\Delta Z^2/2\sigma'^2\right) d\Delta Z \end{aligned} . \tag{A7}$$

where $\alpha \approx \arctan\left(\Delta Z/a\right)$ is defined as the slope angle of the rough surfaces. Because no analytical solution for this equation exists, a numerical plot of $\bar{\alpha}$ is given in figure S3. In addition, rough peaks would shade the outgoing ions/atoms. The shading probability is determined by the mean profile element height of Gaussian-type surface asperities,

$$\overline{\Delta Z} = \frac{\int_0^{3\sqrt{2}\sigma'} \Delta Z \cdot F\left(\Delta Z\right) d\Delta Z}{\int_0^{3\sqrt{2}\sigma'} F\left(\Delta Z\right) d\Delta Z} = \frac{\int_0^{3\sqrt{2}\sigma'} \Delta Z \cdot \exp\left(-\Delta Z^2/2\sigma'^2\right) d\Delta Z}{\int_0^{3\sqrt{2}\sigma'} \exp\left(-\Delta Z^2/2\sigma'^2\right) d\Delta Z} = \sqrt{\frac{2}{\pi}}\sigma' = \frac{2}{\sqrt{\pi}}\sigma . \tag{A8}$$

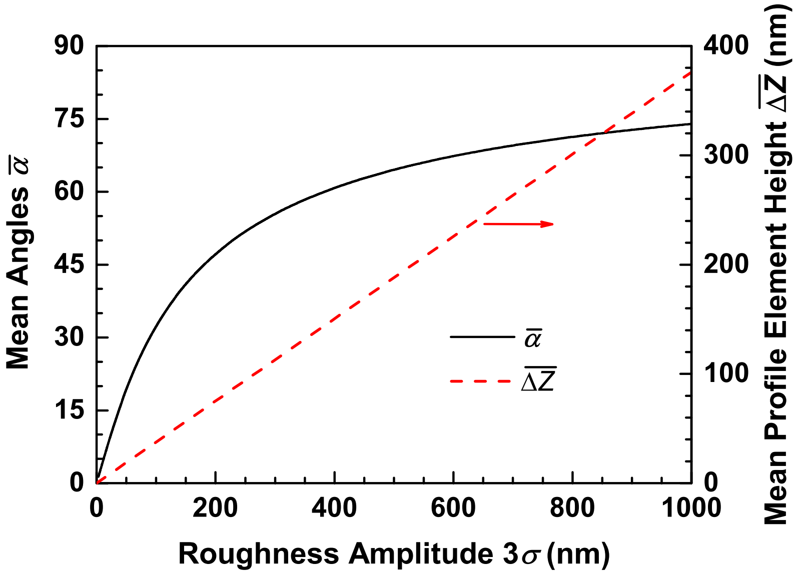

**Figure S3.** Roughness amplitude-dependent mean slope angles of rough surfaces/ion effective incident angles ( $\bar{\alpha}$ ), and the mean profile element height ( $\overline{\Delta Z}$ ) for the shading effects of outgoing ions/atoms.

## S3. Shading probability of rough surfaces

When including the anisotropic effect, the general scheme diagram for ion incidence, reflection, and sputtering from rough surfaces is shown in figure S4. Only the backscattered ions and sputtered atoms exiting within a solid angle Ω can escape from a rough surface. The emission polar angle ($\theta$') range, for ion beam bombardment at a distance $Z$ from rough peaks with an effective incident angle $\bar{\alpha}$, can be given as,

$$\theta' < \left(90^\circ - \bar{\alpha}\right) + \arctan\left[\frac{2a - Z \cdot \tan\left(90^\circ - \bar{\alpha}\right)}{Z}\right]. \tag{A9}$$

The emission probability $p_e^\theta$ at $Z$ can thus be obtained by numerically integrating the anisotropic distribution of outgoing ions/atoms within the solid angle Ω, with a maximum polar angle $\theta'$ and a symmetric azimuthal angle $\phi'$ relative to the symmetry axis of the solid angle Ω. The total emission probability $P_e$ is then obtained by numerically integrating the spatial distribution of ion backscattering and sputtering at normal incidence from zero to the mean profile element height $\overline{\Delta Z}$ of rough peaks. Accordingly, the shading probability is $P_s = 1 - P_e$, as given in figure S5. The shading probability of ion backscattering barely changes with ion types and energies. The shading probability of sputtering is a little higher than that of ion backscattering, due to a more anisotropic distribution of sputtered atoms with the strong memory effect of the incident angle. In contrast, the angular distribution of He ion backscattering is more uniform, as ions with higher energy can penetrate deeper (and more often) into the substrate and collide with multiply substrate atoms, hence losing their memory of the incoming angle [16].

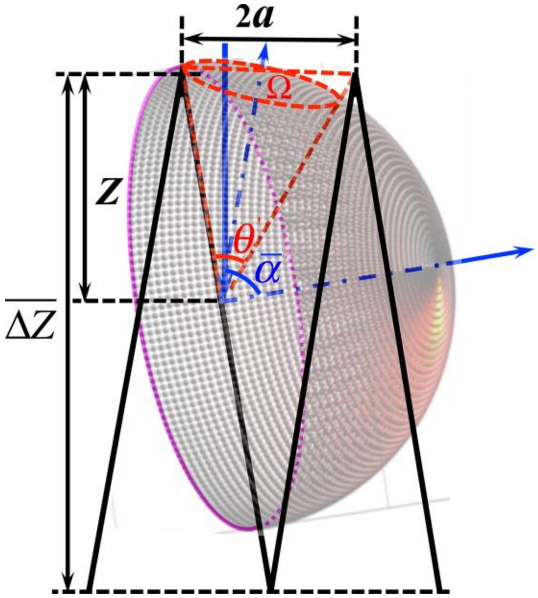

**Figure S4.** Schematic of ion incidence, reflection and sputtering from rough surface. The hemispherical distribution shows the anisotropic outgoing ions.

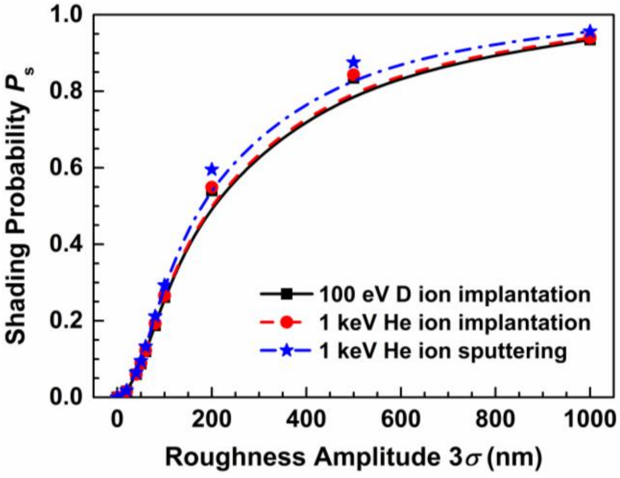

**Figure S5.** Roughness amplitude-dependent shading probability ($P_s$) for the anisotropic distribution of ion backscattering and sputtering, for roughened W under 100 eV D- and 1 keV He-ion irradiation.

## S4. Validation of the relationship between primary retention/sputtering yield and roughness amplitude

In describing the relationship of primary ion retention rates with roughness amplitude, we assume $I_2^0 \approx 1 - h(\bar{a}) + I_1 \cdot h(\bar{a}) \cdot P_s$ ($I_1$ is used as an initial guess) as the secondary retention rate. It should be a good approximation as shown in figure S6. $I_2^0$ is much closer to the actual secondary retention rate (blue line) with roughness amplitude $3\sigma$ for both 100 eV D and 1 keV He ions, at least for large $\sigma$. However, a considerable deviation between $I_2^0$ and the actual secondary retention rate can be found when $3\sigma$ is smaller than about 100 nm. Fortunately, because the shading property at this amplitude region is also vanishing quickly, the contribution of this deviation is suppressed as shown in figures 4 and 5 in the main text.

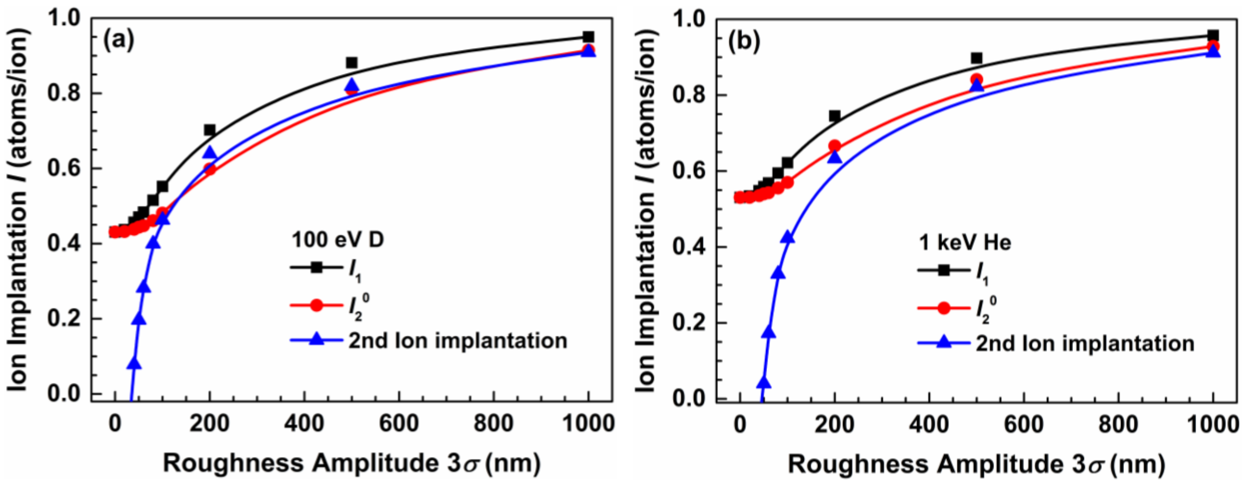

**Figure S6.** Comparison of the ion implantation $I$ of the secondary shading process, for W with different $\sigma$ (a) under 100 eV D- and (b) 1 keV He-ion irradiation. Here, $I_1$ is calculated by equation (3) in the main text, $I_2^0$ is calculated by equation (4) in the main text with $I_1$ as the initial guess, and the actual secondary retention rate (blue line) is calculated by the backward formula of equation (4) with IM3D results.

In describing the relationship between ion sputtering yields ($Y(\bar{\alpha}, \bar{\alpha}')$) and roughness amplitude ($3\sigma$), we set $A(\bar{\alpha}) = 1$ in equation (5) in the main text for simplicity. Indeed, the coefficient $A(\bar{\alpha})$ is rather complex, which is mainly related to the secondary sputtering of backscattered He ions or sputtered W atoms. We neglected this effect in the main text, considering that the emitted atoms will induce less serious surface sputtering when their mean energy is close to/under the threshold energy that can cause W sputtering. Here, we consider the validity of this approximation, by estimating the value of the coefficient $A(\bar{\alpha})$ as the ratio between the values of $Y\left(\bar{\alpha},\bar{\alpha}'\right)$ calculated analytically and by IM3D, as given in figure S7. $A(\bar{\alpha})$ increases with increasing $3\sigma$ quickly, reaching a saturation value after $3\sigma$ = 200 nm. Thus, the secondary sputtering effect induces about 45% extra sputtered atoms for rough W under 1 keV He-ion irradiation.

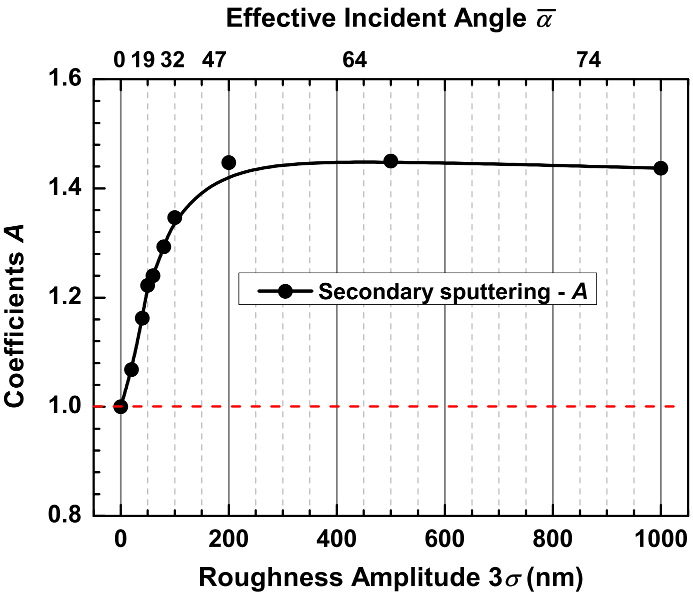

**Figure S7.** Incident-angle dependent coefficient $A(\bar{\alpha})$ (related to the secondary sputtering) with the roughness amplitude ($3\sigma$).

## References

[1] Ren W., Kuronen A. and Nordlund K. 2012 Molecular dynamics of irradiation-induced defect production in GaN nanowires *Phys. Rev. B.* **86** 104114

[2] Bringa E.M. *et al.* 2012 Are nanoporous materials radiation resistant? *Nano. Lett.* **12** 3351-3355

[3] Beyerlein I.J., Caro A., Demkowicz M.J., Mara N.A., Misra A. and Uberuaga B.P. 2013 Radiation damage tolerant nanomaterials *Mater. Today* **16** 443-449

[4] Wirth B.D., Hammond K.D., Krasheninnikov S.I. and Maroudas D. 2015 Challenges and opportunities of modeling plasma–surface interactions in tungsten using high-performance computing *J. Nucl. Mater.* **463** 30-38

[5] Ouyang G., Li X.L., Tan X. and Yang G.W. 2008 Surface energy of nanowires *Nanotech.* **19** 045709

[6] Yang C.C. and Mai Y.W. 2014 Thermodynamics at the nanoscale: A new approach to the investigation of unique physicochemical properties of nanomaterials *Mater. Sci. Eng.: R: Rep.* **79** 1-40

[7] Jiang Q. and Lu H.M. 2008 Size dependent interface energy and its applications *Surf. Sci. Rep.* **63** 427-464

[8] Vanithakumari S.C. and Nanda K.K. 2008 A universal relation for the cohesive energy of nanoparticles *Phys. Lett. A* **372** 6930-6934

[9] Wilhelm R.A., Gruber E., Ritter R., Heller R., Facsko S. and Aumayr F. 2014 Charge Exchange and Energy Loss of Slow Highly Charged Ions in 1 nm Thick Carbon Nanomembranes *Phys. Rev. Lett.* **112** 153201

[10] Biersack J.P. and Haggmark L.G. 1980 A Monte Carlo computer program for the transport of enegetic ions in amorphous targets *Nucl. Inst. Meth.* **174** 257-269

[11] Nanda K.K. 2012 Size-dependent density of nanoparticles and nanostructured materials *Phys. Lett. A* **376** 3301-3302

[12] Yang C.C., Xiao M.X., Li W. and Jiang Q. 2006 Size effects on Debye temperature, Einstein temperature, and volume thermal expansion coefficient of nanocrystals *Solid State Commu.* **139** 148-152

[13] Norgett M.J., Robinson M.T. and Torrens I.M. 1975 A proposed method of calculating displacement dose rates *Nucl. Eng. Des.* **33** 50–54

[14] Stoller R.E., Toloczko M.B., Was G.S., Certain A.G., Dwaraknath S. and Garner F.A. 2013 On the use of SRIM for computing radiation damage exposure *Nucl. Inst. Meth. Phys. Res. B* **310** 75-80

[15] ISO 4287:1997 *Geometrical Product Specifications (GPS)-Surface Texture: Profile Method-Terms, Definitions and Surface Texture Parameters, International Organisation for Standardisation* (Geneva)

[16] Borovikov V., Voter A.F. and Tang X.Z. 2014 Reflection and implantation of low energy helium with tungsten surfaces *J. Nucl. Mater.* **447** 254-270